

Impact Study of AMSR-E Radiances in the NCEP Global Data Assimilation System

MASAHIRO KAZUMORI

*NOAA/NCEP Environmental Modeling Center, and Joint Center for Satellite Data Assimilation, Camp Springs, Maryland, and
Japan Meteorological Agency, Tokyo, Japan*

QUANHUA LIU

Joint Center for Satellite Data Assimilation, Camp Springs, Maryland

RUSS TREADON AND JOHN C. DERBER

NOAA/NCEP Environmental Modeling Center, and Joint Center for Satellite Data Assimilation, Camp Springs, Maryland

(Manuscript received 17 January 2007, in final form 21 May 2007)

ABSTRACT

The impact of radiance observations from the Advanced Microwave Scanning Radiometer for Earth Observing System (AMSR-E) was investigated in the National Centers for Environmental Prediction (NCEP) Global Data Assimilation System (GDAS). The GDAS used NCEP's Gridpoint Statistical Interpolation (GSI) analysis system and the operational NCEP global forecast model. To improve the performance of AMSR-E low-frequency channels, a new microwave ocean emissivity model and its adjoint with respect to the surface wind speed and temperature were developed and incorporated into the assimilation system. The most significant impacts of AMSR-E radiances on the analysis were an increase in temperature of about 0.2 K at 850 hPa at the higher latitudes and a decrease in humidity of about 0.1 g kg^{-1} at 850 hPa over the ocean when the new emissivity model was used. There was no significant difference in the mean 6-h rainfall in the assimilation cycle. The forecasts made from the assimilation that included the AMSR-E data showed small improvements in the anomaly correlation of geopotential height at 1000 and 500 hPa in the Southern Hemisphere and reductions in the root-mean-square error (RMSE) for 500-hPa geopotential height in the extratropics of both hemispheres. Use of the new emissivity model resulted in improved RMSE for temperature forecasts from 1000 to 100 hPa in the extratropics of both hemispheres. The assimilation of AMSR-E radiances data using the emissivity model improved the track forecast for Hurricane Katrina in the 26 August 2005 case, whereas the assimilation using the NCEP operational emissivity model, FAST Emissivity Model, version 1 (FASTEM-1), degraded it.

1. Introduction

Since 2002, the Advanced Microwave Scanning Radiometer for Earth Observing System (AMSR-E) has been observing the atmosphere and surface of the earth using vertically and horizontally polarized radiation at six microwave frequencies from 6.925 to 89 GHz. Other current microwave imagers, such as the Special Sensor Microwave Imager (SSM/I) and Special Sensor Microwave Imager Sounder (SSM/IS), use almost identical

channels in the microwave region, from 19 to 91 GHz. In addition to these channels, AMSR-E has four low-frequency channels in the microwave region (6.925 and 10.65 GHz, dual polarization) that are sensitive to the sea surface wind speed and the sea surface temperature, and are less affected by the atmosphere. Therefore, these measurements provide useful information on the sea surface wind speed and sea surface temperature under almost all weather conditions. The Japan Meteorological Agency (JMA) has been using AMSR-E radiance data in their global data assimilation system since May 2006, and they found it has improved typhoon track predictions and rainfall forecasts (Sato 2006). The purpose of this study is to examine the impact of AMSR-E radiances, including the low-

Corresponding author address: Masahiro Kazumori, Numerical Prediction Division, Japan Meteorological Agency, 1-3-4 Otemachi Chiyoda-ku, Tokyo 100-8122, Japan.
E-mail: kazumori@naps.kishou.go.jp

frequency channels, in the National Centers for Environmental Prediction (NCEP) Global Data Assimilation System (GDAS).

The NCEP GDAS makes use of passive microwave satellite measurements (Derber and Wu 1998; Okamoto and Derber 2006) to improve the accuracy of atmospheric analyses and forecasts. An accurate microwave ocean emissivity model is necessary to assimilate surface sensitive microwave radiances over the ocean. In this research, a scheme to assimilate AMSR-E radiances into the NCEP GDAS was developed, which includes a new microwave ocean emissivity model for AMSR-E low-frequency radiances. The assimilation of AMSR-E radiances is expected to have some impact on the lower troposphere and sea surface in the analyses, as well as on the atmosphere in the forecasts. The impacts of AMSR-E radiance assimilation on the NCEP analyses and forecasts are examined.

In section 2, an overview of the microwave ocean emissivity models is provided and the basis for the new microwave ocean emissivity model is presented. Comparisons of satellite brightness temperature measurements versus calculated values using the emissivity model and the NCEP operational emissivity model [FAST Emissivity Model, version 1 (FASTEM-1); English and Hewison 1998] are shown in section 3. A sensitivity analysis for the microwave ocean emissivity models is shown in section 4. Assimilation experiments examining the impact of AMSR-E radiances are shown in section 5, and conclusions are presented in section 6.

2. Microwave ocean emissivity model

a. Overview

Microwave radiance measurements from satellites contain information from the atmosphere and the surface. To infer geophysical information from these measurements, an atmospheric radiative transfer model and surface emissivity model are required. Since the 1970s, various microwave ocean emissivity models have been suggested. Most of the microwave ocean emissivity models are based on ground-based measurements and/or aircraft measurements.

A two-scale model of the ocean surface has been suggested by Wu and Fung (1972) and Wentz (1975). These models describe the scattering effect of the ocean surface roughness with sufficient accuracy. However, the two-scale models require an integration over the ocean wave spectrum to calculate the microwave ocean emissivity, requiring huge computational resources. Thus, it is difficult to use them in an operational data assimilation system. Therefore, computationally fast ocean emissivity models with sufficient accuracy have

become necessary for operational data assimilation and numerical weather prediction (NWP).

The Community Radiative Transfer Model (CRTM; Weng et al. 2005) previously in the NCEP GDAS used a FASTEM that was the same as the one included in the Radiative Transfer for Television and Infrared Observation Satellite (TIROS) Operational Vertical Sounder (RTTOV), version 6 (Saunders 2000). The FASTEM is similar to FASTEM-1, but the FASTEM has a bug in the calculation of permittivity that affects the emissivity model performance for low-frequency channels. Therefore, we obtained FASTEM-1 code from the model developer and used it for the comparisons in this study.

FASTEM-1 assumes specular reflection and calculates the reflectivity from surface properties (e.g., sea surface temperature, 10-m wind speed). However, FASTEM-2 and -3 use atmospheric transmittance as an input parameter for an effective path correction, which is made during the computation of the downwelling brightness temperature (Deblonde 2000), effectively taking into account nonspecular reflection. The current CRTM does not use atmospheric transmittance as an input for the surface optics calculation. Therefore, it is difficult to use FASTEM-2 (or -3) in the current CRTM. Using FASTEM-2 (or -3) in combination with the CRTM for an impact study in NCEP GDAS is a very interesting topic but is beyond the scope of the AMSR-E impact study.

FASTEM-1 is a semiempirical model, with good performance in the Advanced Microwave Sounding Unit (AMSU) A/B and SSM/I frequency range. However, as shown in section 3, FASTEM-1 has significant errors in the calculation of microwave emissivity at low frequencies (e.g., 6.925 and 10.65 GHz horizontally polarized channels of AMSR-E). Therefore, to assimilate AMSR-E low-frequency channel radiances effectively in the current NCEP GDAS, the development of a new microwave ocean emissivity model is necessary.

A new microwave ocean emissivity model is developed by empirically fitting known physical constraints on the ocean surface emission to the measurements of satellite instruments. The following sections describe the details of this new microwave ocean emissivity model and its derivation. Currently, azimuth angle dependence is not considered in the new model because only vertical and horizontal polarizations are available from AMSR-E measurements. When the full Stokes (Liou 2002) measurements are used (such as WINDSAT on Coriolis) the consideration of azimuth angle dependence, including third and fourth Stokes parameter calculations, is required. And AMSR-E low-frequency channels are affected by Radio Frequency

Interference (RFI). These RFI spots are observed worldwide but seem to be minuscule over the oceans, except near some islands (JAXA 2004).

b. Ocean surface roughness

Microwave ocean emissivity depends on the ocean surface roughness resulting from surface waves that are generated by wind. We adopt a simple two-scale model for the ocean surface roughness. In the two-scale model, a small-scale wave (capillary wave) and a large-scale wave (gravity wave) are used to characterize the complete wave spectrum. The two-scale ocean roughness approximation is commonly used in ocean emissivity models (e.g., Wentz 1975; Wu and Fung 1972) and has shown sufficient accuracy against ground-based and aircraft measurements.

We define the microwave ocean emissivity as

$$\varepsilon_p(\nu, \theta) = 1 - \Gamma_p(\nu, \theta), \quad (p = h \text{ or } v), \quad (1)$$

where $\varepsilon_p(\nu, \theta)$ is the microwave ocean emissivity, $\Gamma_p(\nu, \theta)$ is the total reflectivity of the ocean surface, p denotes either horizontal (h) or vertical (v) polarization, ν is the frequency of radiation, and θ is the incidence angle. Once $\Gamma_p(\nu, \theta)$ is known, the microwave ocean emissivity can be calculated.

In the case of a calm sea, the ocean surface can be considered as a specular surface. The Fresnel reflectivity $R_{p,\text{Fresnel}}$ can be computed using Fresnel's law (Liou 2002) as follows:

$$R_{v,\text{Fresnel}} = \frac{\varepsilon_w \cos \theta - \sqrt{\varepsilon_w - \sin^2 \theta}}{\varepsilon_w \cos \theta + \sqrt{\varepsilon_w - \sin^2 \theta}} \quad \text{and} \quad (2)$$

$$R_{h,\text{Fresnel}} = \frac{\cos \theta - \sqrt{\varepsilon_w - \sin^2 \theta}}{\cos \theta + \sqrt{\varepsilon_w - \sin^2 \theta}}, \quad (3)$$

where ε_w is the complex dielectric constant (permittivity) of water.

When the wind starts blowing, it makes small ripples on the ocean surface. The height variance ς is given by

$$\varsigma^2 = \int_0^\infty S(K) dK, \quad (4)$$

where $S(K)$ is an ocean roughness spectrum function.

The two-scale approach, which separates the waves into large and small scales, is a convenient approximation. A cutoff wavenumber is used for the separation. The method of Liu et al. (1998) defines the small-scale wave as being much smaller than the electromagnetic wave of incident radiation, with the small-scale waves existing on the large-scale wave. The ocean wave spec-

trum from Bjerkaas and Riedel (1979) is used to define an ocean wave spectrum independent of azimuth angle.

The reflectivity is decreased by the diffraction effect by the small-scale waves. To account for this diffraction effect, the refractivity is multiplied by the modified Fresnel coefficient (Guissard and Sobieski 1987):

$$|R_p|^2 = |R_{p,\text{Fresnel}}|^2 \exp(-4k^2 \varsigma_R^2 \cos^2 \theta), \quad (p = h \text{ or } v), \quad (5)$$

where ς_R is the small-scale height variance and $k (=2\pi\nu c^{-1})$ is the wavenumber of electromagnetic radiation; c is the speed of light. An additional correction related to the large-scale waves is still required.

To separate the ocean spectrum into small and large scales, ς_R should satisfy

$$k\varsigma_R \ll 1. \quad (6)$$

With the introduction of the cutoff wavenumber K_c separating the small and large scales, to ensure that the small scale is much smaller than the large scale, K_c must satisfy

$$\frac{K_c}{k} \ll 1. \quad (7)$$

Assuming $k\varsigma_R = K_c k^{-1}$, the small-scale height variance is written as follows:

$$\frac{K_c^2}{k^4} = \varsigma_R^2 = \int_{K_c}^\infty S(K) dK. \quad (8)$$

The cutoff wavenumber K_c is calculated to satisfy the above equation. To reduce computational time, a lookup table for the height variance is used in the calculation.

Note that the small-scale correction is not applied to frequencies below 15 GHz. Preliminary results showed that the difference between the calculated brightness temperature and observed brightness temperature for AMSR-E became larger with the small-scale correction. It is probably not enough to consider only the diffraction effect at frequencies below 15 GHz, since penetration plays an important role in the low-frequency range.

A large-scale correction term is added to modify the large-scale wave refractivity. This term is dependent on incident angle, frequency, and wind speed:

$$|R_v|^2 = |R_{v,\text{Fresnel}}|^2 \exp(-4k^2 \varsigma_R^2 \cos^2 \theta) + W_s(a_1 + a_2\theta + a_3\theta^2)f(\nu) \quad \text{and} \quad (9)$$

$$|R_h|^2 = |R_{h,\text{Fresnel}}|^2 \exp(-4k^2 \varsigma_R^2 \cos^2 \theta) + W_s(b_1 + b_2\theta + b_3\theta^2)f(\nu), \quad (10)$$

where $f(\nu)$ is a function of frequency defined as follows:

$$f(\nu) = \frac{\nu}{c_1 + c_2 \nu}, \quad (11)$$

where $a_1, a_2, a_3, b_1, b_2, b_3, c_1$ and c_2 are constants that are derived from a fit to the satellite measurements in section 2e. At the nadir ($\theta = 0$), the vertical and horizontal reflectivity are required to be the same and, thus, $a_1 = b_1$. Under this model, Eqs. (9) and (10) satisfy Fresnel's law for the calm sea.

In FASTEM-1, the small-scale correction term is included in the diffraction term:

$$|R_p|^2 = |R_{p,\text{Fresnel}}|^2 \exp\left(-\frac{\alpha W_s \cos^2 \theta}{\nu^2}\right), \quad (p = h \text{ or } v), \quad (12)$$

where α is a constant and W_s is the 10-m wind speed. The small-scale correction term is also not applied below 15 GHz in FASTEM-1. The large-scale correction terms are then defined as quadratic functions of the 10-m wind speed and the frequency. However, the Fresnel law for calm seas is not maintained with the coefficients as currently defined.

c. Permittivity

The permittivity (dielectric constant) is one of the basic input parameters for the ocean surface emissivity calculation. Below the microwave frequency region of 20 GHz, the effect of salinity on the permittivity is not negligible. Klein and Swift (1977) presented the permittivity as a function of frequency and water temperature as well as salinity, based on laboratory measurements. Klein and Swift used measurements at 1.43 and 2.653 GHz to derive the coefficients of their permittivity model. Their model has sufficient accuracy for the low-frequency range of microwaves and has been used in numerous applications for many years.

However, as several authors have discussed (Meissner and Wentz 2004; Guillou et al. 1998), the accuracy of the Klein–Swift model is insufficient beyond the 10-GHz frequency region. Ellison et al. (2003) presents an extrapolated model based on a new measurement of permittivity from 20 to 105 GHz. Klein–Swift's model uses the single Debye model for low frequencies while Ellison's model uses the double Debye model for the high frequencies to represent the permittivity. Although the double Debye model has not yet been established theoretically, the model describes the permittivity from 20 to 105 GHz well.

Salinity cannot be neglected below 20 GHz. To take this effect into account, our model uses Guillou's permittivity model below 20 GHz and Ellison's model

above 20 GHz. In FASTEM-1, Ellison's model is used for the entire microwave frequency range. There are discontinuities between Ellison's model and Guillou's at 20 GHz, as shown in Fig. 1. But the discontinuities are small when compared with the dynamic ranges of permittivity. In the assimilation experiment, we also assume that the models are used for discrete frequencies rather than continuous frequencies. We think the discontinuities at 20 GHz do not affect this study.

d. Foam emissivity and foam fraction

Foam emissivity and foam fraction on the ocean surface are important factors under strong wind conditions. Foam emissivity and coverage both increase the emissivity and the brightness temperature measured by satellite microwave instruments. To incorporate the effects of foam on the emissivity under strong wind conditions, accurate foam emissivity, and foam fraction models are both needed.

Stogryn (1972) derived an empirical sea foam emissivity model as a function of frequency, incidence angle, and sea surface temperature from previously published radiometric measurements as follows:

$$\varepsilon_{p,\text{Foam}}(\nu, \theta) T_w = \varepsilon_{p,\text{Foam}}(\nu, 0) T_w F_v(\theta), \quad (p = h \text{ or } v), \quad (13)$$

$$\varepsilon_{p,\text{Foam}}(\nu, 0) T_w = 208 + 1.29\nu, \quad (14)$$

$$F_h(\theta) = 1 - 1.748 \times 10^{-3} \theta - 7.336 \times 10^{-5} \theta^2 + 1.044 \times 10^{-7} \theta^3, \quad \text{and} \quad (15)$$

$$F_v(\theta) = 1 - 9.946 \times 10^{-4} \theta + 3.218 \times 10^{-5} \theta^2 - 1.187 \times 10^{-6} \theta^3 + 7 \times 10^{-20} \theta^{10}, \quad (16)$$

where $\varepsilon_{p,\text{Foam}}(\nu, \theta)$ is the foam emissivity, T_w is the sea surface temperature in kelvins, ν is frequency expressed in GHz, and θ is the incidence angle in degrees.

The foam emissivity for vertical and horizontal polarizations are the same at the nadir ($\theta = 0$) because of the isotropy of the foam. A recent study by Rose et al. (2002) shows that the measurements of foam emissivity at 10.8 and 36.5 GHz are greater than the Stogryn (1972) foam emissivity model calculations. According to their measurements, the measured foam emissivity is greater than 0.9 over a range of incidence angles between 30° and 60° for the vertical polarization, while the horizontally polarized emissivity is lower than the vertical polarized emissivity and gradually decreases as the incidence angle increases. Based on these new mea-

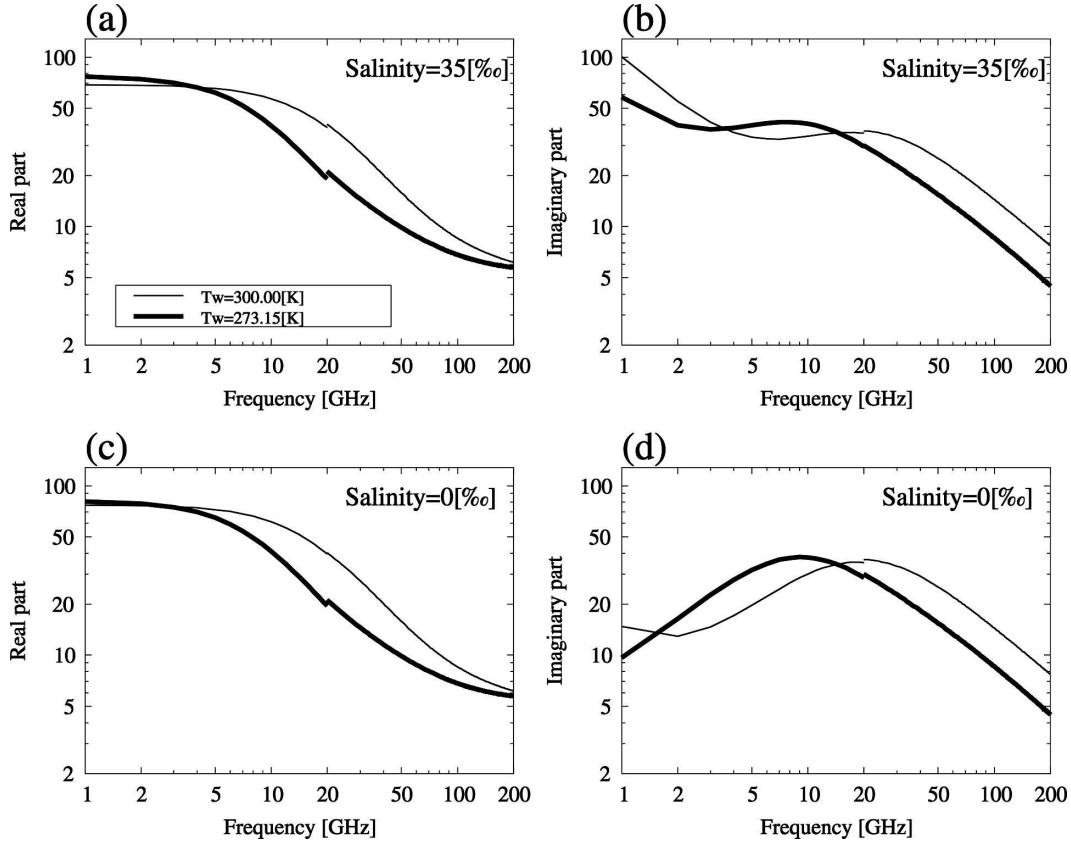


FIG. 1. The permittivity from the Ellison et al. (2003) model (above 20 GHz) and Guillou et al. (1998) (below 20 GHz). (a), (c) The real part (salinity 35‰ and 0‰, respectively), and (b), (d) the imaginary part. Thick and thin lines are for water temperature 300.00- and 273.15-K cases, respectively.

measurements of the foam emissivity, we modified Stogryn's foam emissivity model. The foam emissivity at the nadir is set to 0.93 in our new model and the constant value (0.93) is used for vertical polarization at all incidence angles. The same incident angle dependence that Stogryn (1972) derived is used for the horizontal polarization. Figure 2 shows the Stogryn foam emissivity and modified foam emissivity as a function of incident angle. The reflectivity of the foam is calculated from the foam emissivity by using the following:

$$|R_{p,\text{Foam-covered}}(\nu, \theta)|^2 = 1 - \varepsilon_{p,\text{Foam}}(\nu, \theta), \quad (p = h \text{ or } v). \quad (17)$$

FASTEM-1 uses a constant value (1.0) for the foam emissivity for both polarizations over all incidence angles. The constant value (1.0) of foam emissivity for the horizontal polarization seems large and may be the cause of the bias in horizontal polarization in FASTEM-1, seen in section 3.

The foam fraction also varies depending on wind

speed. Several empirical models of foam fraction have been suggested. The Wisler and Hollinger (1977) function is given by

$$f = 7.751 \times 10^{-6} u^{3.231}, \quad (18)$$

where f is foam fraction and u is the 10-m wind speed in meters per second. The foam fraction is expressed by a power law of wind speed. Our new emissivity model adopts the Wisler–Hollinger function with the foam fraction set to zero when wind speed is below 7 m s^{-1} .

FASTEM-1 uses the Monahan and O'Muircheartaigh (1986) function:

$$f = 1.95 \times 10^{-5} u^{2.55} \exp(0.0861 \Delta T), \quad (19)$$

where ΔT is a low-elevation atmospheric stability used in Monahan and O'Muircheartaigh (1986). Here ΔT is set to zero in FASTEM-1. Figure 3 shows a comparison of the two foam fraction functions. The functions are similar below 10 m s^{-1} wind speed; however, the differences become large at high wind speed conditions.

The total reflectivity of the ocean surface $\Gamma_p(\nu, \theta)$ can

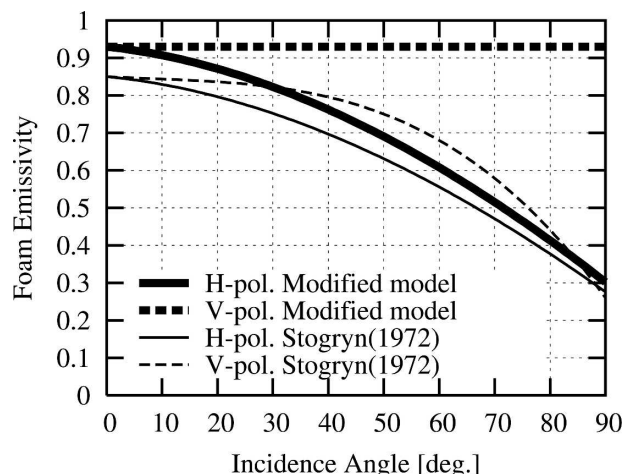


FIG. 2. The Stogryn foam emissivity and modified foam emissivity functions (thin lines and thick lines, respectively). Solid lines are for the horizontal polarization, and broken lines are for vertical polarization. The incidence angle of AMSR-E is 55° (54.5° for 89.0 GHz).

be calculated from the foam fraction f and reflectivities of the foam-free and foam-covered parts, using

$$\Gamma_p(\nu, \theta) = f |R_{p, \text{Foam-covered}}(\nu, \theta)|^2 + (1 - f) |R_{p, \text{Foam-free}}(\nu, \theta)|^2 \quad (p = h \text{ or } v). \quad (20)$$

e. Emissivity estimation from satellite measurements

Most emissivity models are empirically adjusted based on aircraft measurements and/or ground-based measurements. We have empirically tuned our emissivity model by fitting the satellite measurements and by using the CRTM for the atmospheric radiative transfer calculations.

Based on a plane-parallel approximation (Janssen 1993), the brightness temperature $T_b(\nu, \theta)$ at the top of atmosphere is written as

$$T_b(\nu, \theta) = T_u(\nu, \theta) + \{\varepsilon_s(\nu, \theta) T_s + [1 - \varepsilon_s(\nu, \theta)] T_d(\nu, \theta)\} e^{-\tau_{\text{sec}} \theta}, \quad (21)$$

where $T_u(\nu, \theta)$ is the upwelling atmospheric brightness temperature, $T_d(\nu, \theta)$ is the downwelling atmospheric brightness temperature, T_s is the surface temperature, $e^{-\tau_{\text{sec}} \theta}$ is the atmospheric transmittance, and ε_s is the ocean surface emissivity. Here $T_u(\nu, \theta)$, $T_d(\nu, \theta)$, and $e^{-\tau_{\text{sec}} \theta}$ are calculated by using the CRTM, and T_s is obtained from the NCEP operational SST analysis. The ocean emissivity is derived from this equation. The atmospheric input profiles for the CRTM are obtained from the operational NCEP atmosphere analysis. Mi-

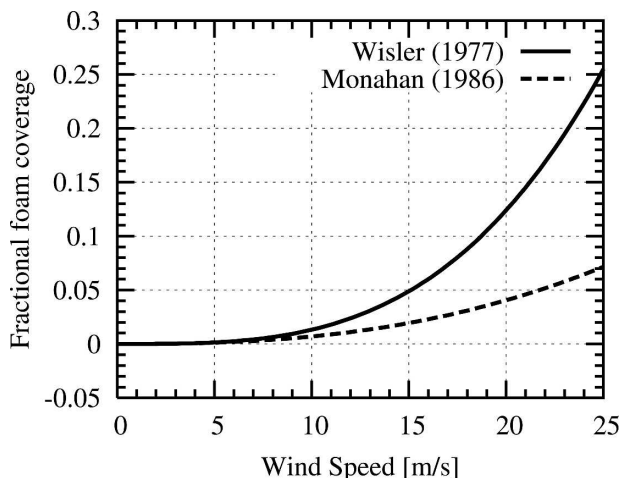


FIG. 3. A comparison of fractional foam coverage models. The solid line is for Wisler and Hollinger (1977), which is used in the new model, and the broken line is for Monahan and O'Muircheartaigh (1986), which is used in FASTEM-1.

crowave radiance measurements from AMSU-A on the National Oceanic and Atmospheric Administration (NOAA) satellites *NOAA-15* and *NOAA-16*, from SSM/I on the Defense Meteorological Satellite Program (DMSP) *DMSP-13*, *DMSP-14*, and *DMSP-15*, and from AMSR-E on *Aqua* are used for the fits. Clear-sky measurements are selected based on the retrieved cloud liquid water (CLW; Grody et al. 1999; Weng and Grody 1994; Yan and Weng 2004). The threshold of CLW was set at 0.01 kg m^{-2} .

Mixed polarized emissivity ε_m can be expressed in terms of the polarization angle $\theta_{\text{polarization}}$. For vertical polarization at the nadir position, ε_m at scan angle θ_{scan} is

$$\varepsilon_m = \cos^2 \theta_{\text{polarization}} \varepsilon_v + \sin^2 \theta_{\text{polarization}} \varepsilon_h, \quad (22)$$

where $\theta_{\text{polarization}} = \theta_{\text{scan}}$ or $\theta_{\text{polarization}} = 90 - \theta_{\text{scan}}$, depending on the polarization status at the nadir, and ε_v and ε_h are the emissivity of vertical and horizontal polarization, respectively. To include the mixed polarization of AMSU-A data in the coefficient estimation, we use Eq. (22) to derive the coefficients. The right-hand side of Eq. (22) is used as the predictor in the regression. Atmospheric profiles, surface properties of the GDAS analysis, and microwave radiance measurements from 18 December 2005 were used to derive the coefficients. The derived coefficients are summarized in Table 1.

3. Comparison of the emissivity models

To compare the new emissivity model (NEWMDL) and FASTEM-1, AMSR-E brightness temperatures

TABLE 1. The coefficients of the large-scale correction.

Vertical polarization		Horizontal polarization		Frequency	
a_1	2.616×10^{-5}	b_1	-2.616×10^{-5}	c_1	1.91
a_2	1.407×10^{-5}	b_2	-1.389×10^{-5}	c_2	0.12
a_3	-1.738×10^{-7}	b_3	-6.106×10^{-8}		

were calculated by using CRTM and the two emissivity models. The input profiles (temperature, humidity, and ozone) and surface properties (sea surface temperature and 10-m wind speed) were obtained from 6-h global forecasts of the NCEP GDAS. The emissivity models were evaluated over the period of 1–5 December 2005, resulting in more than 15 000 comparisons for each channel. The calculated AMSR-E brightness temperatures were compared with the measurements. Clear-sky measurements were selected using a CLW threshold of 0.01 kg m^{-2} . The bias of calculated brightness temperature (T_{Bcal})–observed brightness temperature (T_{Bobs}) should be slightly negative if the cloud effect is not removed completely.

Figure 4 shows the results. For the horizontal polarization (Fig. 4a), the biases in low-frequency channels (6.925 and 10.65 GHz) are substantially reduced in the NEWMDL. At high-frequency channels, the bias and standard deviation of NEWMDL are comparable with FASTEM-1, except at 23.8 GHz. The bias of vertically polarized channels (Fig. 4b) is smaller than that of horizontally polarized channels. The difference between the two models is also smaller for vertical polarization. The biases at 23.8 GHz (for both polarizations) of NEWMDL are slightly worse than those of FASTEM-1. Because these channels are located near the moisture absorption line of the microwave frequency range, the increased bias might be caused by insufficient accuracy in the analyzed moisture field.

To understand the large differences in the biases of the horizontally polarized low-frequency channels, it would be helpful to present scatterplots of the brightness temperature difference ($T_{\text{Bcal}} - T_{\text{Bobs}}$) versus 10-m wind speed. The radiative transfer model (CRTM) uses atmospheric profiles (e.g., temperature, humidity, and ozone) and surface parameters (e.g., surface type, surface temperature, and surface wind speed for the ocean) as inputs for the calculation of brightness temperature. Wind speed is used for the ocean emissivity model in the CRTM and ocean emissivity determines the surface radiation in the radiative transfer calculation. Therefore, the wind speed–dependent bias in the calculated brightness temperature can be considered an indicator showing the performance of the ocean emissivity model. Figure 5 shows the scatterplot of AMSR-E 10.65-GHz horizontal polarization for NEWMDL (Fig. 5a) and FASTEM-1 (Fig. 5b). Clearly, the bias increases in both models when wind speeds become large. However, NEWMDL has a smaller bias compared with FASTEM-1 at high wind speeds. Since wind speed is not a predictor in the current GSI radiance bias correction scheme (Okamoto and Derber 2006), it is unlikely that this bias can be properly removed without improving the calculated brightness temperatures with an improved emissivity model.

4. Sensitivity analysis

In this section, the sensitivity of brightness temperature to sea surface temperature and wind speed are computed for AMSR-E channels using NEWMDL and FASTEM-1. The sensitivity of the brightness temperatures to geophysical parameters is a good indicator of the available information on the geophysical parameters in that observation.

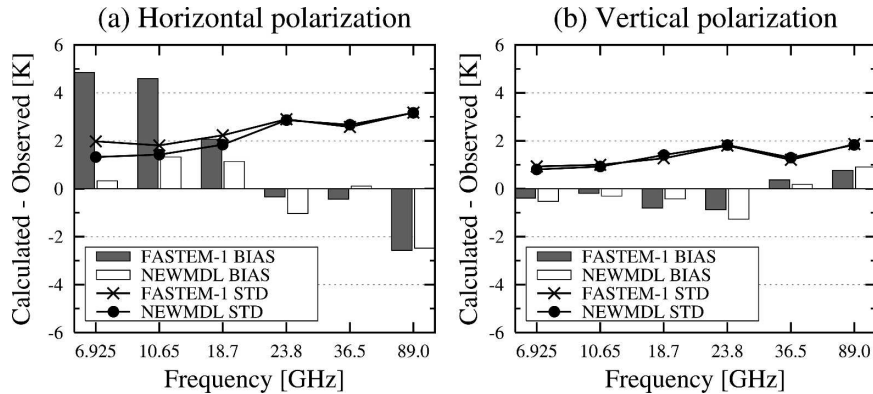


FIG. 4. The brightness temperature comparison between the calculations and measurements of AMSR-E channels: (a) horizontal polarization and (b) vertical polarization. These statistics were calculated for the period 1–5 Dec 2005.

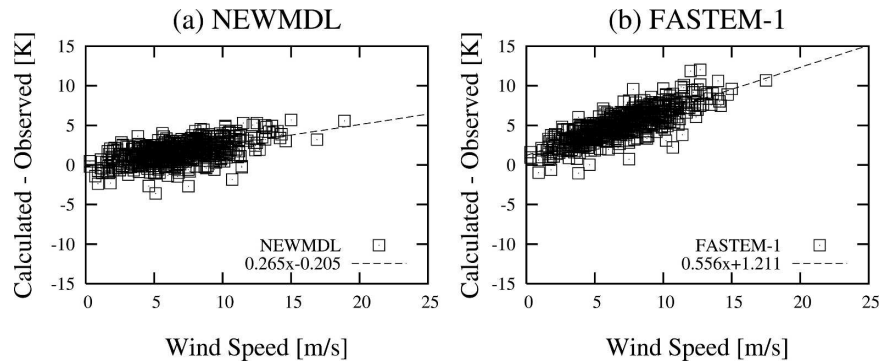


FIG. 5. Scatterplots of AMSR-E 10.65-GHz horizontally polarized brightness temperature difference ($TB_{cal} - TB_{obs}$) vs 10-m wind speed from the 6-h forecast from (a) NEWMDL and (b) FASTEM-1. The fitted linear function is also shown by the broken line in (a) and (b). These statistics were calculated from the data (total precipitable water in the range 30–40 $kg\ m^{-2}$ and SST in the range 285–295 K) for the period 1–5 Dec 2005.

The typical sensitivity to sea surface temperature and wind speed are obtained by globally averaging all AMSR-E radiance data over the ocean from the 1200 UTC 23 October 2005 GDAS analysis. Because the foam parameterization in the emissivity models has a wind speed dependency, the datasets are divided into two categories (wind speed at and above $7\ m\ s^{-1}$, or below $7\ m\ s^{-1}$). Table 2 shows the sensitivity to sea surface temperature of the AMSR-E channels, and Tables 3 and 4 show the sensitivity to sea surface wind speed. The important points from this sensitivity analysis are summarized as follows:

- The vertically polarized channels are more sensitive to sea surface temperature than the horizontally polarized channels. The AMSR-E 6.925-GHz vertically polarized channel has the largest sensitivity to sea surface temperature. The measurements from the 6.925-GHz vertical polarization channel have more information on sea surface temperature than those from other channels. NEWMDL and FASTEM-1 have similar sensitivity to sea surface temperature for all channels.

TABLE 2. Sensitivity of AMSR-E brightness temperature to the SST for vertical polarization (V) and for horizontal polarization (H).

Frequency (GHz) polarization	NEWMDL ($K\ K^{-1}$)		FASTEM-1 ($K\ K^{-1}$)	
	V	H	V	H
6.925	0.56	0.26	0.54	0.26
10.65	0.46	0.20	0.43	0.20
18.7	0.23	0.07	0.19	0.05
23.8	0.11	0.00	0.11	0.00
36.5	0.01	−0.09	0.00	−0.10
89.0	0.10	−0.09	0.09	−0.10

- The horizontally polarized channels are more sensitive to surface wind speed. Generally, FASTEM-1 has a larger sensitivity to the sea surface 10-m wind speed than NEWMDL (wind speed below $7\ m\ s^{-1}$, in particular).
- The horizontally polarized channels have a larger sensitivity to surface wind speed above $7\ m\ s^{-1}$ than surface wind speed below $7\ m\ s^{-1}$ in both models.

The sensitivity to sea surface wind speed for the horizontally polarized channels may be excessive in FASTEM-1 at low-frequency channels (6.925 and 10.65 GHz). Other research (Deblonde 2000; Okamoto and Derber 2006) has also pointed out an excess sensitivity in the SSM/I horizontally polarized channel at the lower frequency of 19 GHz.

5. Assimilation experiments

a. Design of the experiments

To examine the impact of AMSR-E radiance on analyses and forecasts, the NCEP GSI analysis system

TABLE 3. Sensitivity of AMSR-E brightness temperature to the sea surface wind speed for $W_s < 7\ m\ s^{-1}$.

Frequency (GHz) polarization	NEWMDL [$K\ (m\ s^{-1})^{-1}$]		FASTEM-1 [$K\ (m\ s^{-1})^{-1}$]	
	V	H	V	H
6.925	−0.16	0.69	0.90	2.80
10.65	−0.21	0.90	0.36	1.93
18.7	−0.43	0.68	0.05	1.33
23.8	−0.40	0.46	−0.01	0.94
36.5	−0.49	0.75	−0.11	1.33
89.0	−0.26	0.64	−0.17	0.66

TABLE 4. Sensitivity of AMSR-E brightness temperature to the sea surface wind speed for $W_s \geq 7 \text{ m s}^{-1}$.

Frequency (GHz) polarization	NEWMDL [K (m s ⁻¹) ⁻¹]		FASTEM-1 [K (m s ⁻¹) ⁻¹]	
	V	H	V	H
6.925	0.35	1.17	1.02	2.91
10.65	0.28	1.34	0.49	2.06
18.7	-0.04	1.07	0.16	1.49
23.8	-0.06	0.92	0.07	1.13
36.5	-0.14	1.17	-0.02	1.26
89.0	-0.17	0.88	-0.14	0.81

(Wu et al. 2002) and the NCEP global forecast model (as of May 2006) were employed. The operational resolution of T382L64 (wavenumber 382 triangular truncation with 64 vertical sigma levels) was used for these experiments. A total of 168-h forecasts were produced daily from the analysis at 0000 UTC during the experiment period. Three data assimilation experiments were conducted for one month (12 August–11 September 2005). The three experiments include a control (Cntl) using all the operational observation data; a Test1 adding the AMSR-E data and using FASTEM-1; and a Test2, which is the same as Test1 except that NEWMDL is used for frequencies below 20 GHz. The operational observation dataset includes surface wind data [i.e., buoy, ship, retrieved SSM/I wind speed data, and Quick Scatterometer (QuikSCAT) wind vector data] and other microwave radiance data [AMSU-A from *NOAA-15*, *-16*, *-18*, and *Aqua*; AMSU-B from *NOAA-15*, *-16*, and *-17*; Microwave Sounding Unit (MSU) from *NOAA-14*; and Microwave Humidity Sounder (MHS) from *NOAA-18*], but none of those channels are below 20 GHz. Therefore, the only differences between Test1 and Test2 result from the use of NEWMDL for the AMSR-E low-frequency channels. It is difficult to see a clear impact from AMSR-E if NEWMDL were applied to all microwave radiance data. Comparisons of Cntl and Test1 (and Test2) will demonstrate the impact of AMSR-E, while differences between Test1 and Test2 will show the impact of using NEWMDL with the AMSR-E low-frequency channels.

The AMSR-E radiances (10.65, 18.7, 23.8, and 36.5 GHz at both polarizations) are assimilated in Test1 and Test2. The 6.925-GHz channels are not used because

the size of the field of view (FOV; $43.2 \text{ km} \times 75.4 \text{ km}$) is much larger than the resolution of the analysis field (about 50 km). The AMSR-E 89-GHz channel has two scans (Kawanishi et al. 2003), 89-GHz-A and 89-GHz-B. The 89-GHz-B scan uses a different off-nadir angle resulting in a different observation location. Therefore, assimilating the 89-GHz-B channel together with other channels is difficult. The 89-GHz-A scan data were not available for the both experiment periods due to instrument trouble.

b. Quality control of AMSR-E radiances

Because of the huge volume of raw AMSR-E data and the difficulty of explicitly treating observation error correlations for time and space in a data assimilation system, data thinning is a convenient method for selecting the proper data for the assimilation. AMSR-E data are thinned to $160 \text{ km} \times 160 \text{ km}$ boxes over the oceans. The cloud- and rain-affected AMSR-E radiances are excluded in the quality control procedures. Although the CRTM has an ability to simulate cloudy radiances, the quality of the cloud/rain simulations is uncertain and the proper techniques for using these data are still under development.

To detect the presence of rain and cloud, the same method as in SSM/I quality control (Okamoto and Derber 2006) was used. Rejection criteria were set based on the amount of CLW (Yan and Weng 2004) for each channel (Table 5). For the low-frequency channels, the thresholds are higher than for high-frequency channels because the higher-frequency channels are more sensitive to cloud. The observation errors of AMSR-E channels were set at $\frac{2}{3}$ of the standard deviation of $TB_{\text{cal}} - TB_{\text{obs}}$ (Okamoto and Derber 2006). These values were calculated from the 1–5 December 2005 dataset and are listed in Table 5. As the size of the FOV of AMSR-E low-frequency channels is relatively large compared to the high-frequency channels, the size of the FOV should be taken into account in the AMSR-E data processing to screen the contamination of cloud or land (ice) in the FOV. The small-size FOV data (36.5-GHz channels) inside the large-size FOV data (10.65-GHz channels) are used to detect cloud or land contamination. Since some of the low-frequency measurements from the ascending orbit in the Southern Hemisphere

TABLE 5. Thresholds of CLW amount (kg m^{-2}) and observation error σ_0 (K) for AMSR-E channels.

Frequency (GHz) polarization	10.65		18.7		23.8		36.5	
	V	H	V	H	V	H	V	H
σ_0 (K)	0.73	0.95	0.92	1.20	1.17	1.84	0.84	1.60
CLW (kg m^{-2})	0.35		0.3		0.25		0.1	

are affected by a sun glint effect, these data are also excluded based on a sun glint angle ($\leq 25^\circ$) in the quality control procedure. The same radiance bias correction scheme is used with the current GSI scheme (Okamoto and Derber 2006). CLW retrieval is used as one of the predictors in the bias correction scheme to partially correct for residual cloud effects.

Figure 6 shows histograms of AMSR-E brightness temperature differences ($TB_{\text{cal}} - TB_{\text{obs}}$). Cloud-affected data are excluded, and the biases seem to be properly corrected. The frequency distributions are close to the normal distribution. Figures 7 and 8 show the horizontal distribution of brightness temperature differences ($TB_{\text{cal}} - TB_{\text{obs}}$) for the AMSR-E channels used. The left-hand side panels show figures prior to the bias correction and the right-hand side panels after bias correction. For the 36.5-GHz channels, a negative bias remains in the high-latitude areas after bias correction and may indicate either real information or inadequacies in the bias correction for these channels. The bias correction has two parts—one is scan dependent and the other is airmass dependent. The former is not as dependent on geophysical location for these channels. The latter is estimated from five predictors using a linear regression. The predictors, set to be constant, are scan angle ($=0$ for AMSR-E), cloud liquid water, integrated weighted lapse rate, and its square. The coefficients are optimized for each channel in the analysis and then used for the next analysis in the assimilation cycle. The same coefficients are used globally. Therefore, the remaining bias in the 36.5-GHz channels may represent insufficient background accuracy in the lower tropospheric temperature and/or surface wind speed in the high latitudes. As wind speed is not included as a predictor in this scheme, using a different predictor (wind speed and/or sea surface temperature) might show better performance. Improving the radiance bias correction scheme is big issue. But, in general, the results suggest that the data selection, quality control procedures, and bias correction are working properly.

c. Experimental results

1) IMPACTS ON ANALYSIS

Because the AMSR-E measurements use microwave window channels, the information should be concentrated in the surface wind speed, temperature, and moisture in the lower troposphere. Figures 9a,b shows the zonal mean distribution of the root-mean-square (RMS) of the wind speed analysis increment at the lowest sigma level (0.9973). Figures 9c,d shows the RMS difference from the Cntl. The reduction in the lowest-

level wind speed increments indicates smaller differences from the 6-h forecast and, thus, an improvement in the first-guess wind speed. The improvement is located in the high latitudes of the Southern Hemisphere for the Test2 case, with a smaller impact in Test1 than Test2.

Changes in temperature and moisture in the lower troposphere of the analysis were also found. Figure 10 shows the averaged 850-hPa temperature difference from the Cntl run during the experiment period. Figure 11 shows the averaged specific humidity difference from the Cntl run. In Test1, there were no significant differences in the averaged analysis fields. However, an increase in temperature (about 0.2 K) in the high latitudes (Fig. 10b) and a decrease in the humidity (about 0.1 g kg^{-1}) over the oceans (Fig. 11b) were found in Test2. The area of decreased humidity is limited to the ocean; in particular, to the dry area outside of the intertropical convergence zone (ITCZ). This is a reasonable result because the clear or thin cloud radiances were assimilated in these experiments. Generally, impacts on the analysis from AMSR-E radiances were found over the oceans in data-sparse areas. Therefore, it was difficult to capture these impacts from fits to radiosonde observations (RAOBs) or in comparisons with other conventional observations. There was no significant differences in the mean 6-h rain rate for either experiment, but a slight reduction in the first-guess mean total precipitable water bias was found in the Southern Hemisphere.

2) IMPACTS ON FORECAST

Although the impacts of the assimilation of AMSR-E radiances on analyses were primarily over limited areas of the Southern Hemisphere and oceanic regions, the forecast impacts are found over larger regions. Figure 12 shows the anomaly correlation coefficients in the extratropics (latitudes 20° – 80°N/S) for 1000- and 500-hPa geopotential heights. Impacts in the Northern Hemisphere were almost neutral while significant improvements (about 1% for the 5-day forecasts) were found in the Southern Hemisphere in both experiments. Ratios of cases where the anomaly correlation coefficients are larger in Test2 than the Cntl over the total number of cases (31 for the initial time and 24 for the 168-h forecast) are also shown in Fig. 12 by histograms. The ratios for the Southern Hemisphere exceed 50% for all forecast hours.

As for the verification of forecast wind fields, the fits to RAOB for the 24- and 48-h wind vector forecasts were calculated. In the Northern Hemisphere and tropics, there was no significant difference in either experiment. However, slight improvements were found in the

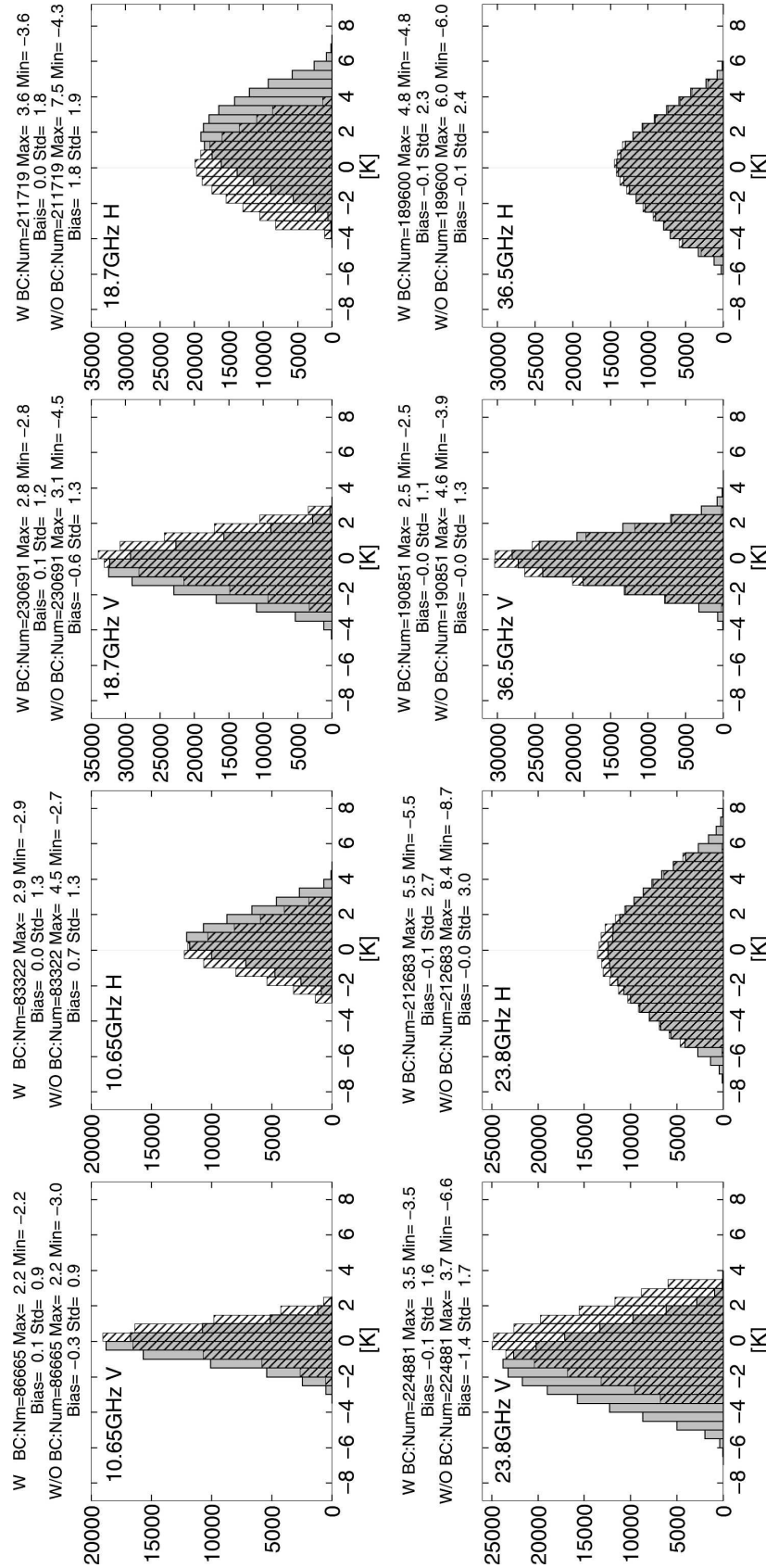


FIG. 6. The histograms of AMSR-E brightness temperature differences between the calculated brightness temperature ($T_{B_{cal}}$) and observed brightness temperature ($T_{B_{obs}}$). The histograms are for AMSR-E radiance data that passed the quality control in Test2. The statistics were calculated for the period 12 Aug–11 Sep 2005. The gray histograms are for the data without bias correction, and hatched histograms are for data with bias correction. The statistics (data number, maximum, minimum, bias, and std dev) are shown.

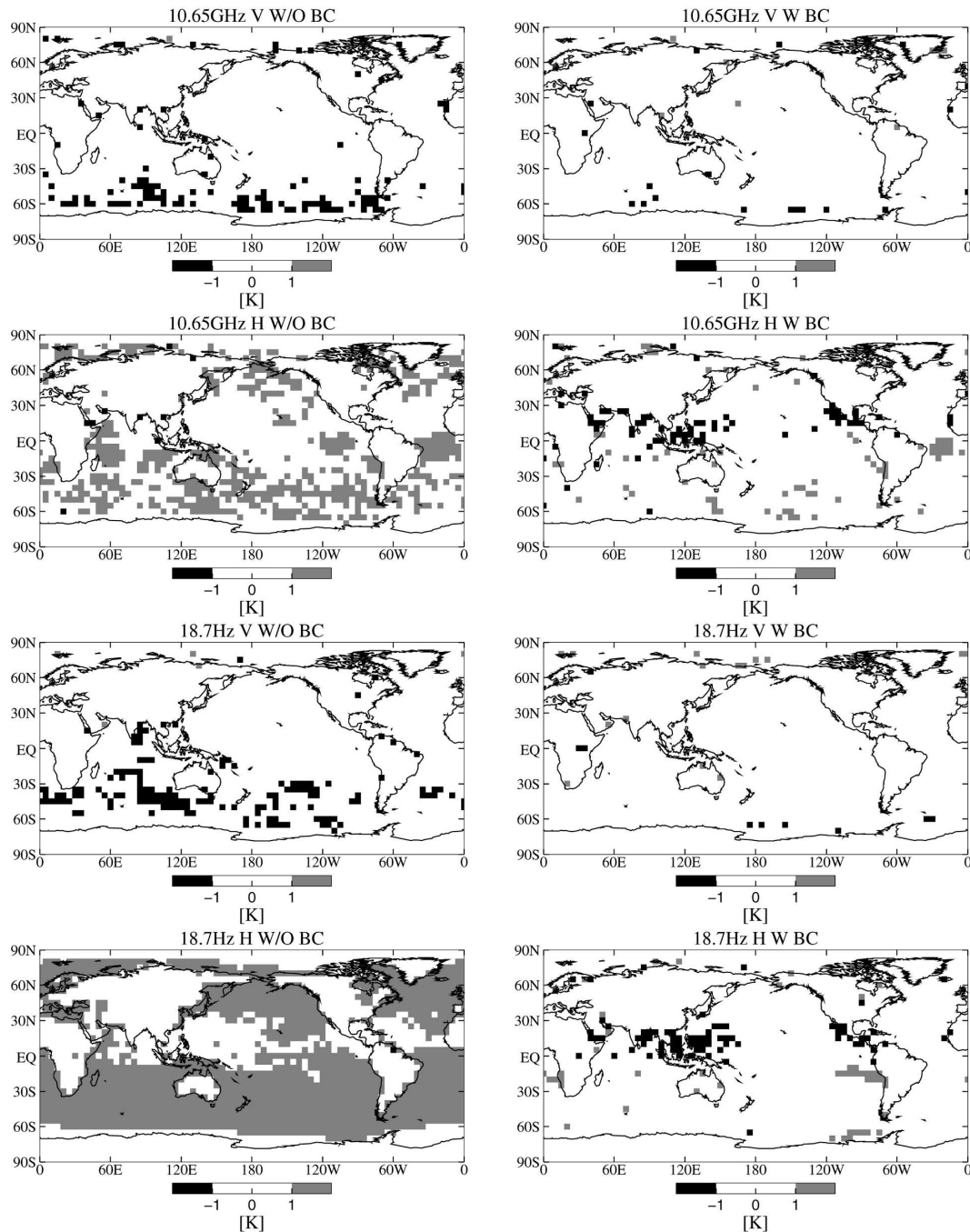


FIG. 7. Horizontal distribution of the AMSR-E brightness temperature differences ($TB_{cal} - TB_{obs}$) from Test2 (left) without bias correction and (right) with bias correction for both polarizations at 10.65 and 18.7 GHz. The period is for 12 Aug–11 Sep 2005, and the grid size is $5^\circ \times 5^\circ$.

lower troposphere and around the 300-hPa height in the Southern Hemisphere (Fig. 13). For other geophysical parameters, such as temperature, moisture, and geopotential height, similar improvements were confirmed in the Southern Hemisphere.

Figures 14a,b show zonal mean RMSE of 500-hPa geopotential height for 5-day forecasts. The errors were calculated against their own analysis. In Figs. 14c,d, their differences from the Cntl were shown with negative values indicating a forecast improvement. Im-

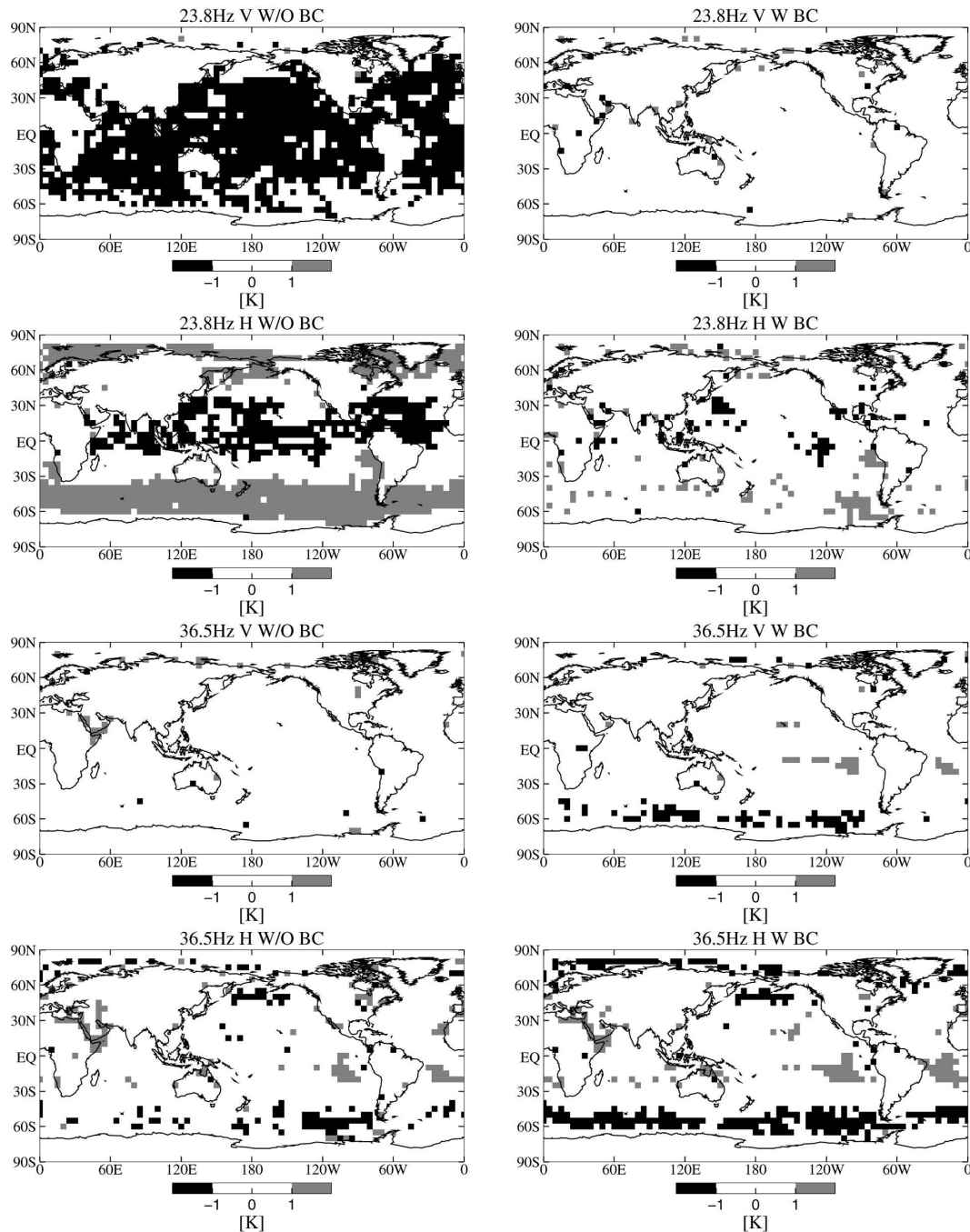


FIG. 8. As in Fig. 7, but at 23.8 and 36.5 GHz.

provements in the extratropics were clearly found in both experiments.

Figures 15a,b show zonal mean RMSE of the 5-day temperature forecast from 1000 to 100 hPa. Figures 15c,d show their RMSE difference from the Cntl with the negative values indicating a forecast improvement. The improvements in Test2 were generally larger than those in Test1.

Consistent impacts on the analysis and forecast in another experiment period (1–21 December 2005) were obtained. During the former experiment period (12 August–11 September 2005), a hurricane (Katrina) existed in the northern Gulf of Mexico. In 2005, Katrina was an extraordinarily strong hurricane (Knabb et al. 2005) and caused serious damage in the United States. As a case study, we examined the track prediction from

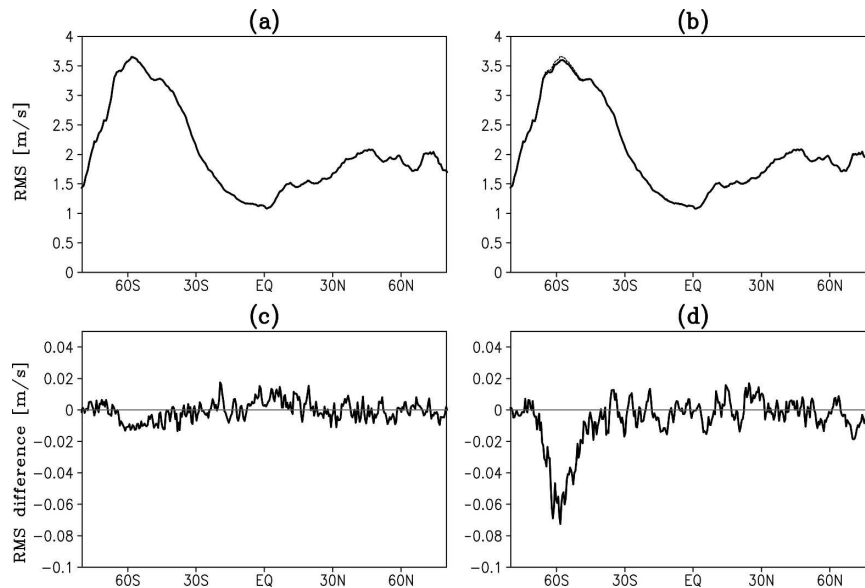


FIG. 9. The zonal mean distribution of the RMS of the wind speed analysis increment at the lowest sigma level (0.9973): (a) Test1 and (b) Test2. The solid lines in (a) and (b) are Test1 (or Test2), and the broken lines are for the Cntl run. The difference from the Cntl for (c) Test1 and (d) Test2. The statistics are computed for the period of 12 Aug–11 Sep 2005.

each experiment. Figure 16 shows the comparison of the hurricane track predictions (0000 UTC initial forecasts). Katrina reached the hurricane stage by 0000 UTC 26 August and continued as a hurricane through 1800 UTC 29 August. The forecasts from 0000 UTC 25 August initial field have large errors for Cntl, Test1, and Test2. The errors were not improved when AMSR-E radiances were assimilated in the experiments. However, differences in the track prediction were found in the 26 and 27 August cases. In the 26 August case, an improvement was found in Test2 while Test1 degraded the forecast relative to the Cntl. In

the 27 August case, both experiments degraded the forecast accuracy but Test2 showed a slightly better result than Test1. It is clear that there are an insufficient number of cases to determine any clear signal concerning hurricane track forecasts from these results.

6. Conclusions

In this study, a new microwave ocean emissivity model was developed for use in the assimilation of AMSR-E low-frequency channels. The new microwave ocean emissivity model was a two-scale model empiri-

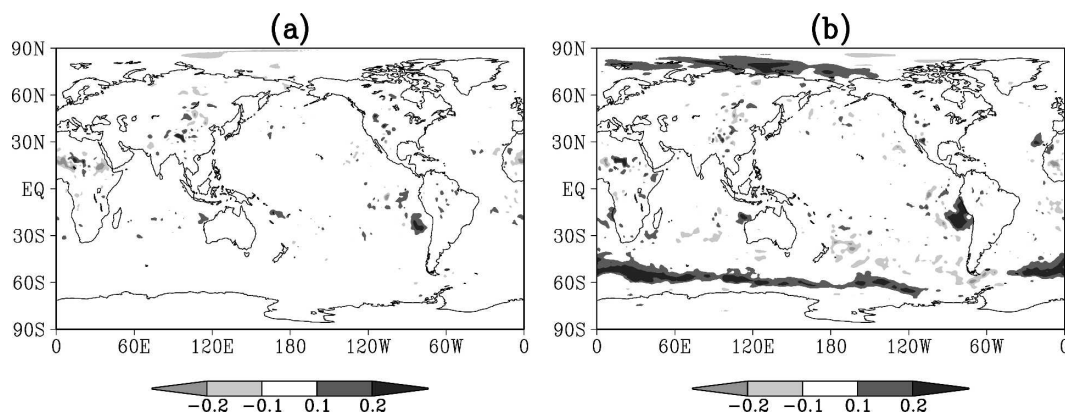
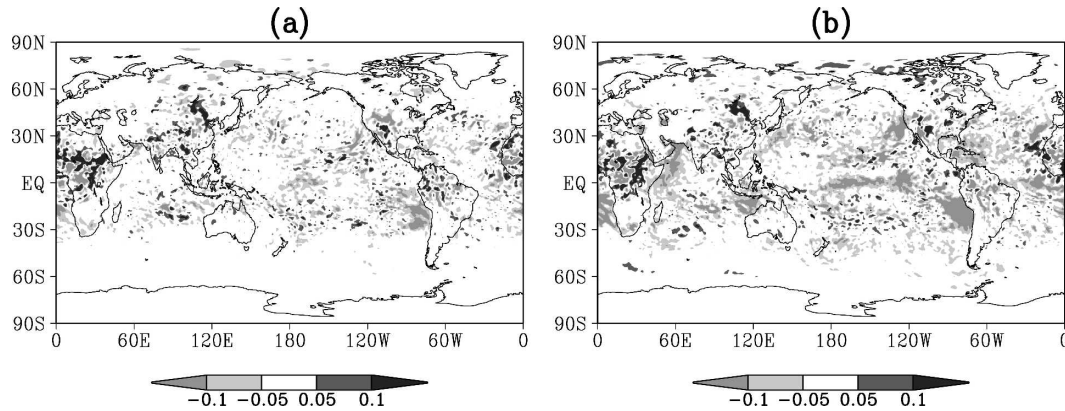


FIG. 10. Averaged 850-hPa temperature difference (K) between the Test1 (or Test2) and Cntl runs: (a) Test1 and (b) Test2. The statistical period is 12 Aug–11 Sep 2005.

FIG. 11. As in Fig. 10, but for specific humidity (g kg^{-1}).

cally tuned to satellite measurements. Comparisons of the calculated brightness temperatures with observations indicated that the new emissivity model performs better at low frequencies. A clear reduction of the wind-dependent bias was seen in the AMSR-E 10.65-GHz horizontally polarized channel. The sensitivity study showed that FASTEM-1 and the new emissivity model had a similar sensitivity to the sea surface temperature in the 6.925–89-GHz microwave frequencies. However, the new model had a much weaker sensitivity

to surface wind speeds than FASTEM-1. A quality control procedure for AMSR-E radiances was developed for the data assimilation. To exclude cloud- and rain-contaminated data, it was necessary to consider the size of the FOV for low-frequency channels because they have a much larger FOV. The 6.925-GHz channels were not used because their FOV ($43.2 \text{ km} \times 75.4 \text{ km}$) was larger than the resolution of the analysis (about 50 km).

In the assimilation experiments, the impact of

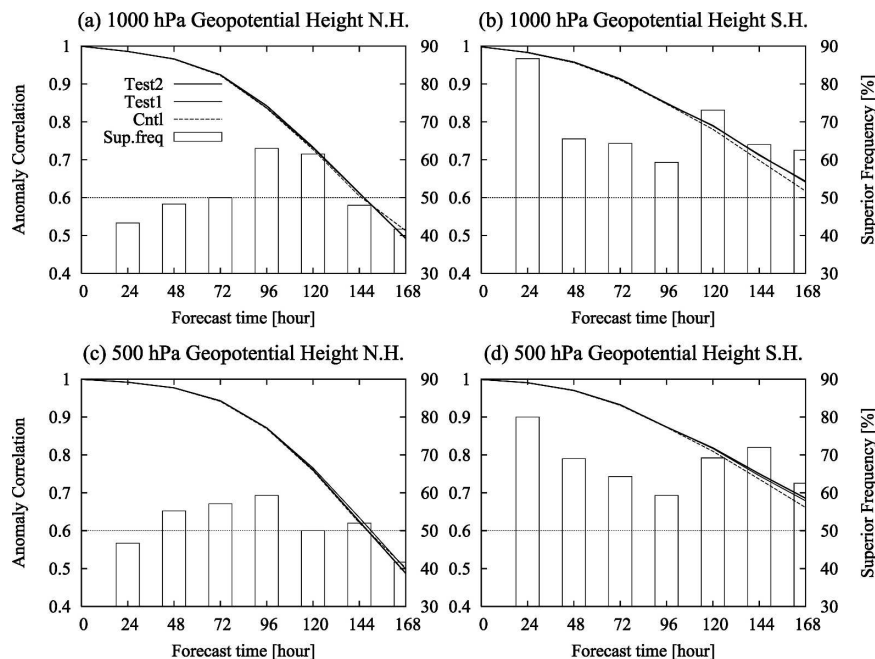


FIG. 12. Averaged anomaly correlation coefficient at 1000 hPa in the (a) Northern Hemisphere and (b) Southern Hemisphere and at 500 hPa in the (c) Northern Hemisphere and (d) Southern Hemisphere. The statistics are computed for 12 Aug–11 Sep 2005, with 31 cases at the initial time and 24 cases for the 168-h forecast. Histograms represent the ratio of number of Test2 cases superior to the Cntl, with the scale given on the right axis.

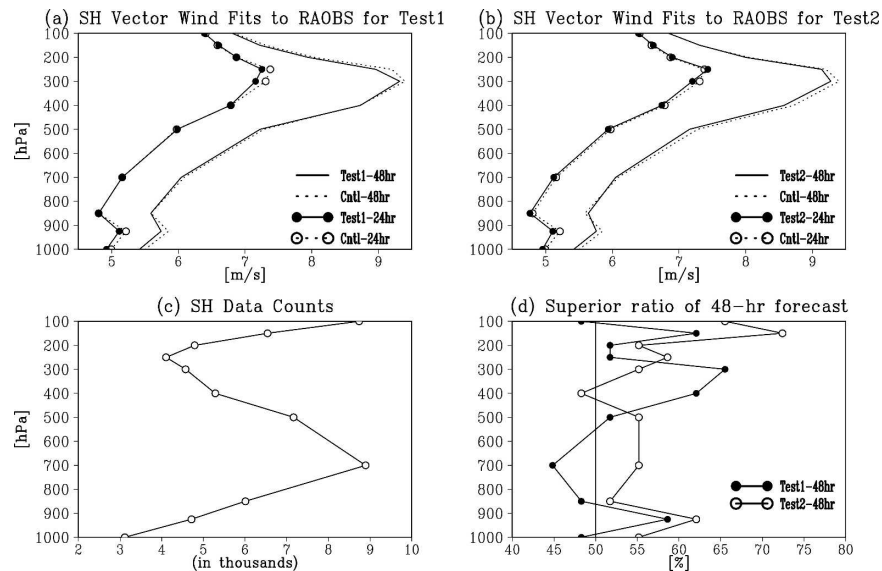


FIG. 13. Vertical profiles of the RMSE of the 24- and 48-h forecasts for vector wind (m s^{-1}) verified against radiosonde observations in the Southern Hemisphere. Vertical axis units: hPa. The statistics are computed for 0000 UTC 14 Aug–0000 UTC 11 Sep 2005: (a) Test1 and (b) Test2. The Cntl run statistics are shown by dotted lines, and those from Test1 (or Test2) are shown by solid lines. The RMSEs of the 24-h forecast are shown with a circle, and those of the 48-h forecast are shown by the lines without a circle. (c) The RAOB data counts and (d) the ratio of the number of test cases superior to the Cntl for the 48-h forecast with a black (or white) circle for Test1 (or Test2).

AMSR-E radiances on the surface wind speed analysis appeared to be limited to the Southern Hemisphere high latitudes. Because the operational dataset already included many surface wind-related data [i.e., retrieved SSM/I wind speed data (Yu et al. 1997) and QuikSCAT

wind data (Yu 2003)], the ability to improve the near-surface wind analysis over the ocean could be limited. The new emissivity model resulted in an increase in temperature (about 0.2 K) at 850 hPa in the high latitudes. AMSR-E radiances produced a decrease in hu-

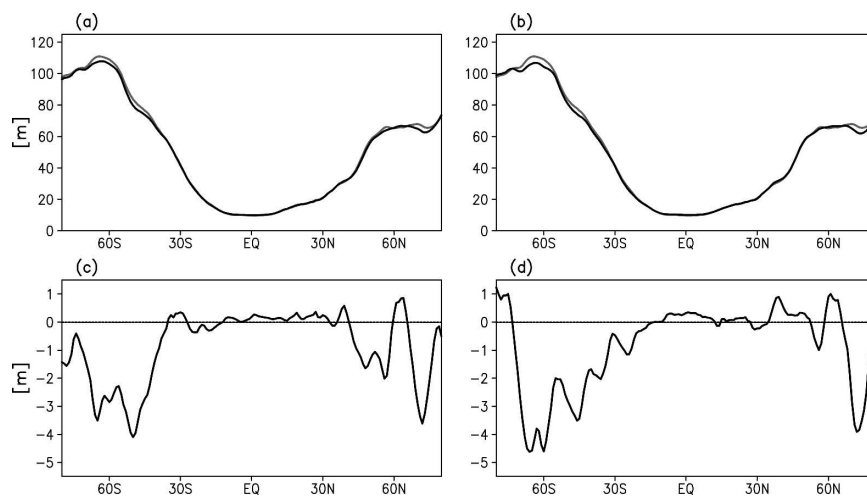


FIG. 14. Zonal mean RMSE of the 500-hPa geopotential height for the 5-day forecast for (a) Test1 and (b) Test2. The gray line is the Cntl, and the black line is Test1 (or Test2). The errors were calculated against their own analysis. Also shown are the RMSE differences from the Cntl for (c) Test1 and (d) Test2. The period for these statistics is 17 Aug–11 Sep 2005.

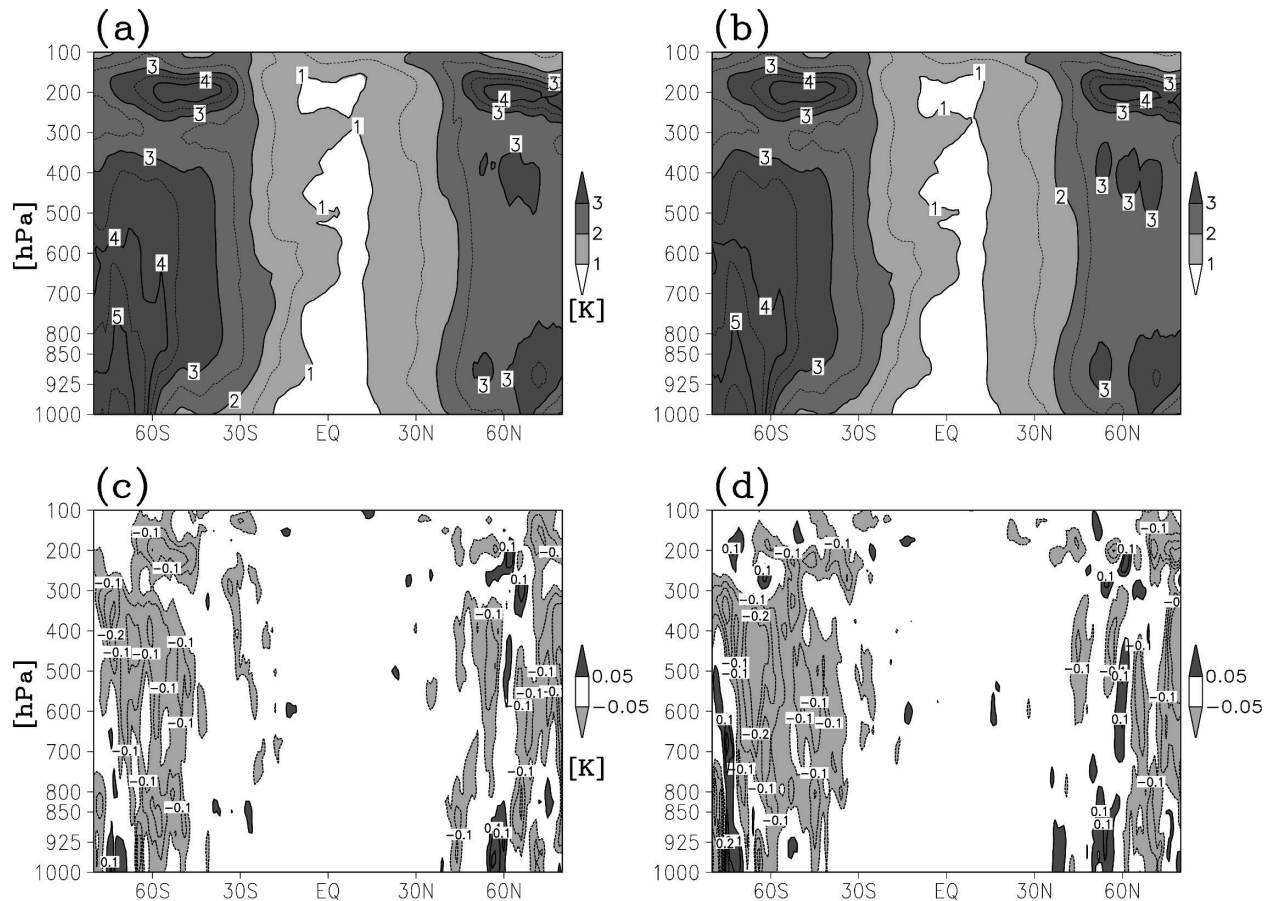


FIG. 15. Zonal mean RMSE of the 5-day temperature forecast from 1000 to 100 hPa for (a) Test1 and (b) Test2 and the difference in RMSE from the Cntl for (c) Test1 and (d) Test2. The period is 17 Aug–11 Sep 2005.

midity with the new emissivity model giving a larger decrease than that from FASTEM-1. The humidity decrease was limited to the low CLW and low humidity area outside of the ITCZ and made no difference in mean 6-h rainfall in the assimilation cycle. This result was reasonable because only clear and thin-cloud AMSR-E radiance data were assimilated in the experiments. Although the impact from limited usage of AMSR-E radiance data was small, including the cloudy radiances (through the use of clouds in the radiative transfer) could bring about larger impacts in the tropics.

The forecast anomaly correlation scores of geopotential height at 500 and 1000 hPa were improved in the Southern Hemisphere in both experiments (Test1 and Test2). These results indicated that AMSR-E radiances bring a positive impact to the Southern Hemisphere no matter which emissivity model was used. Neutral impacts in the tropics and the Northern Hemisphere (slightly positive) were found. Because most of the impacts on the analysis of surface wind speed and tem-

perature were limited to the high latitudes of the Southern Hemisphere, the impacts on midlatitude forecasts appeared at a later stage of the forecast range. The decreases of RMSE in the 500-hPa geopotential height and temperature forecasts from 1000 to 100 hPa were also confirmed. A larger improvement was obtained when the new emissivity model was used. These results suggested that the analysis of surface wind speed and temperature in the high latitudes is an important factor in improving the forecast score. We obtained a consistent impact on the analysis and forecast in another experiment period (1–21 December 2005). In the case study of Hurricane Katrina in 2005, no significant improvement was found, while the use of FASTEM-1 for AMSR-E radiances actually degraded the track prediction. The assimilation of AMSR-E radiance data with the new emissivity model improved the track forecast for Hurricane Katrina in the 26 August 2005 case.

In conclusion, AMSR-E radiance assimilation using the new emissivity model impacted both analyses and forecasts. These results suggest that the use of

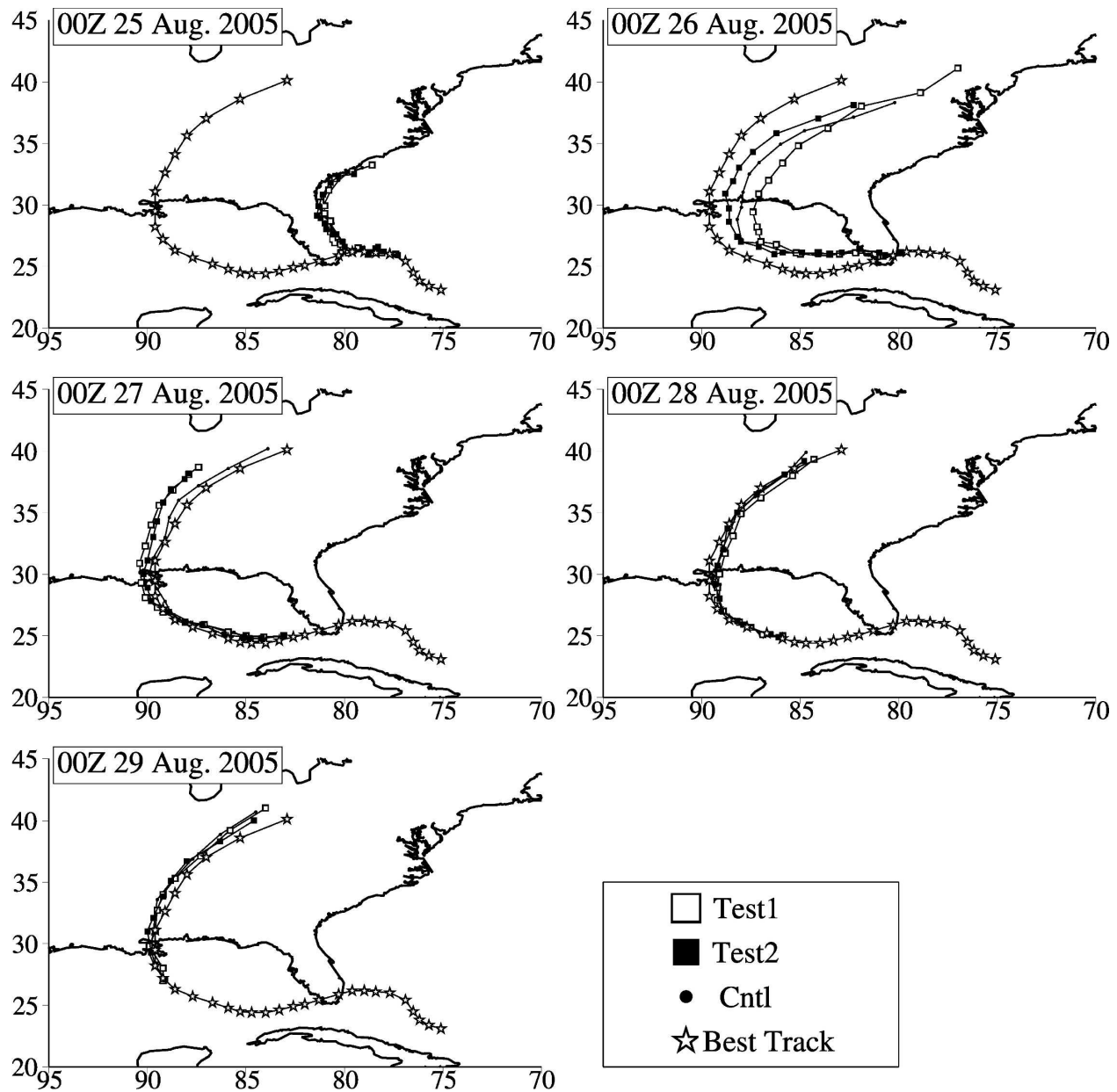


FIG. 16. Comparison of hurricane track predictions for Katrina in 2005. The samples are from the 0000 UTC initial forecast for 25–29 Aug 2005. The symbols show the center of the hurricane every 6 h.

AMSR-E radiances will bring some improvement to the NCEP operational NWP system, and the new emissivity model can effectively extract information about the ocean surface from AMSR-E low-frequency channels.

Acknowledgments. This study was carried out under the collaboration of NOAA/NCEP and JMA, supported by the University of Maryland. The authors acknowledge Profs. Antonio J. Busalacchi and Phillip Arkin for their encouragement and support. Special

thanks are given to Drs. Stephen J. Lord and John Le Marshall who provided the opportunity of this study in JCSDA, Dr. Fuzhong Weng for his insightful comments in this study, and Dr. Steve English who provided the FASTEM-1 code. We also thank two anonymous referees for their helpful comments.

REFERENCES

- Bjerkaas, A. W., and F. W. Riedel, 1979: Proposed model for the elevation spectrum of a wind-roughened sea surface. Tech. Memo. TG1328, Applied Physics Laboratory, The Johns Hopkins University, Laurel, MD, 31 pp.

- Deblonde, G., 2000: Evaluation of FASTEM and FASTEM2. NWP SAF Rep. NWPSAF-MO-VS-001, version 1.0, NWP Satellite Application Facility, Met Office, 53 pp.
- Derber, J. C., and W.-S. Wu, 1998: The use of TOVS cloud-cleared radiances in the NCEP SSI analysis system. *Mon. Wea. Rev.*, **126**, 2287–2299.
- Ellison, W. J., and Coauthors, 2003: A comparison of ocean emissivity models using the Advanced Microwave Sounding Unit, the Special Sensor Microwave Imager, the TRMM Microwave Imager, and airborne radiometer observations. *J. Geophys. Res.*, **108**, 4663, doi:10.1029/2002JD003213.
- English, S. J., and T. J. Hewison, 1998: A fast generic millimeter-wave emissivity model. *Microwave Remote Sensing of the Atmosphere and Environment*, T. Hayasaka et al., Eds., International Society for Optical Engineering (SPIE Proceedings Vol. 3503), 288–300.
- Grody, N., F. Weng, and R. Ferraro, 1999: Application of AMSU for obtaining water vapor, cloud liquid water, precipitation, snow cover and sea ice concentration. *Technical Proc. 10th Int. ATOVS Study Conf.*, Boulder, CO, WMO, 230–240.
- Guillou, C., W. Ellison, L. Eymard, K. Lamkaouchi, C. Prigent, G. Delbos, G. Balana, and S. S. Boukabara, 1998: Impact of new permittivity measurements on sea surface emissivity modeling in microwaves. *Radio Sci.*, **33**, 649–667.
- Guisard, A., and P. Sobieski, 1987: An approximate model for the microwave brightness temperature of the sea. *Int. J. Remote Sens.*, **8**, 1607–1627.
- Janssen, M. A., 1993: *Atmospheric Remote Sensing by Microwave Radiometry*. Wiley Series in Remote Sensing, John Wiley and Sons, 572 pp.
- JAXA, cited 2004: Caveats of L1B brightness temperature product (version 1.0). [Available online at http://sharaku.eorc.jaxa.jp/AMSR/data_re/amsre/tp040331_e.htm.]
- Kawanishi, T., and Coauthors, 2003: The Advanced Microwave Scanning Radiometer for the Earth Observing System (AMSR-E), NASDA's contribution to the EOS for global energy and water cycle studies. *IEEE Trans. Geosci. Remote Sens.*, **41**, 184–194.
- Klein, L. A., and C. T. Swift, 1977: An improved model for the dielectric constant of sea water at microwave frequencies. *IEEE J. Oceanic Eng.*, **OE-2** (1), 104–111.
- Knabb, R. D., J. R. Rhome, and D. P. Brown, 2005: Hurricane Katrina. Tropical Cyclone Rep. TCR-AL12200S, National Hurricane Center, Miami, FL, 42 pp.
- Liou, K. N., 2002: *An Introduction to Atmospheric Radiation*. 2nd ed. Academic Press, 583 pp.
- Liu, Q., C. Simmer, and E. Ruprecht, 1998: Monte Carlo simulations of the microwave emissivity of the sea surface. *J. Geophys. Res.*, **103** (C11), 24 983–24 989.
- Meissner, T., and F. J. Wentz, 2004: The complex dielectric constant of pure and sea water from microwave satellite observations. *IEEE Trans. Geosci. Remote Sens.*, **42**, 1836–1849.
- Monahan, E. C., and I. G. O'Muircheartaigh, 1986: Whitecaps and the passive remote sensing of the ocean surface. *Int. J. Remote Sens.*, **7**, 627–642.
- Okamoto, K., and J. C. Derber, 2006: Assimilation of SSM/I radiance in the NCEP global data assimilation system. *Mon. Wea. Rev.*, **134**, 2612–2631.
- Rose, L. A., and Coauthors, 2002: Radiometric measurements of the microwave emissivity of foam. *IEEE Trans. Geosci. Remote Sens.*, **40**, 2619–2625.
- Sato, Y., 2006: Operational use of AMSR-E radiance data in the JMA global analysis. Joint AMSR Science Team Meeting, La Jolla, CA, 28 pp. [Available online at http://www.ghcc.msfc.nasa.gov/AMSR/meetings2006/pdf_science/sato-AMSR-PI-WS2006.pdf.]
- Saunders, R. W., 2000: RTTOV-6—Science and validation report. EUMETSAT, 31 pp. [Available online at <http://www.metoffice.gov.uk/research/interproj/nwpsaf/rtm/d81svr.pdf>.]
- Stogryn, A., 1972: The emissivity of sea foam at microwave frequencies. *J. Geophys. Res.*, **77**, 1658–1666.
- Weng, F., and N. C. Grody, 1994: Retrieval of cloud liquid water using the special sensor microwave imager (SSM/I). *J. Geophys. Res.*, **99** (D12), 25 535–25 551.
- , Y. Han, P. van Delst, Q. Liu, T. Kleespies, B. Yan, and J. Le Marshall, 2005: JCSDA Community Radiative Transfer Model (CRTM). *Proc. 14th Int. TOVS Study Conf.*, Beijing, China, Int. TOVS Working Group, 217–221.
- Wentz, F. J., 1975: A two-scale scattering model for foam-free sea microwave brightness temperatures. *J. Geophys. Res.*, **80**, 3441–3446.
- Wisler, M. M., and J. P. Hollinger, 1977: Estimation of marine environmental parameters using microwave radiometric remote sensing systems. NRL Memo. Rep. 3661, Naval Research Laboratory, Washington, DC, 27 pp.
- Wu, S. T., and A. K. Fung, 1972: A noncoherent model for microwave emissions and backscattering from the sea surface. *J. Geophys. Res.*, **77** (30), 5917–5929.
- Wu, W.-S., R. J. Purser, and D. F. Parrish, 2002: Three-dimensional variational analysis with spatially inhomogeneous covariances. *Mon. Wea. Rev.*, **130**, 2905–2916.
- Yan, B., and F. Weng, 2004: Hydrological parameters derived from Aqua AMSR-E measurements. Preprints, *13th Conf. on Satellite Meteorology and Oceanography*, Norfolk, VA, Amer. Meteor. Soc., P8.17.
- Yu, T.-W., 2003: Operational use of QuikSCAT winds in NCEP GDAS. Preprints, *12th Conf. on Satellite Meteorology and Oceanography/12th Conf. on Interactions of the Sea and Atmosphere*, Long Beach, CA, Amer. Meteor. Soc., JP4.7.
- , M. Iredell, and D. Keyser, 1997: Global data assimilation and forecast experiments using SSM/I wind speed data derived from a neural network algorithm. *Wea. Forecasting*, **12**, 859–865.